Supporting Information

Belt-Shaped π-Systems: Relating Geometry to Electronic Structure in a Six-Porphyrin Nanoring

Johannes K. Sprafke, Dmitry V. Kondratuk, Michael Wykes, Amber L. Thompson, Markus Hoffmann, Rokas Drevinskas, Wei-Hsin Chen, Chaw Keong Yong, Joakim Kärnbratt, Joseph E. Bullock, Marc Malfois, Michael R. Wasielewski, Bo Albinsson, Laura M. Herz, Donatas Zigmantas, David Beljonne and Harry L. Anderson

Table of Contents

Department of Chemistry, University of Oxford, Chemistry Research Laboratory
12 Mansfield Road, Oxford OX1 3TA (United Kingdom)
Fax: (+44) 1865 285 002; E-mail: harry.anderson@chem.ox.ac.uk

Chemistry of Novel Materials, University of Mons
Place du Parc 20, B-7000 Mons (Belgium)
Fax: (+32) 65 373 861; E-mail: david.beljonne@umons.ac.be

Department of Chemical Physics, Lund University (Sweden)

Department of Chemistry, Department of Chemical and Biological Engineering, Physical Chemistry, Kemivägen 3, SE-41296 Göteborg (Sweden)

Department of Chemistry and Argonne-Northwestern Solar Energy Research (ANSER) Center, Northwestern University, Evanston, Illinois 60208-3113 (USA)

Diamond Light Source Ltd, Harwell Science and Innovation Campus, Didcot OX11 ODE (United Kingdom)

Clarendon Laboratory, Department of Physics, University of Oxford,
Parks Road, Oxford OX1 3PU (United Kingdom)

Section S1. Materials, Methods and Instrumentation

All manipulations of air or water sensitive compounds were performed using standard high-vacuum techniques. When required, solutions were degassed by boiling under reduced pressure followed by saturating with N_2; this cycle was then repeated. Dry THF, CH_2Cl_2 and toluene were obtained by passing through alumina under N_2 pressure. All other reagents were used as commercially supplied. NMR data were collected at 500 MHz using a Bruker AVII 500 or at 400 MHz using a Bruker DPX 400 at 298 K. Chemical shifts are quoted as parts per million (ppm) relative to residual $CHCl_3$ at δ 7.27 ppm and coupling constants (*J*) are reported in Hertz. MALDI-ToF spectra were measured using a Waters MALDI micro or at the EPSRC National Mass Spectrometry service (Swansea) using the Applied Biosystems Voyager DE-STR. Room temperature UV-vis-NIR absorbance measurements were recorded with a Perkin-Elmer Lambda 20 photospectrometer. Room temperature fluorescence spectra were recorded using an automated custom-built system consisting of a 75 W xenon lamp focused into a monochromator, which then illuminated the sample in a quartz fluorescence cell. A silicon photodiode was used to normalize the incident excitation intensities. Luminescence from the sample was collected at 90 ° to the excitation beam and focused into a spectrograph fitted with a liquid nitrogen cooled InGaAs photodiode array. The spectral response of the detector was corrected by using a standard tungsten lamp (OL 245U, Optronic Laboratories Inc.). The linear porphyrin hexamer **Si$_2$-*l*-P'6** (Φ_f = 8.0% in toluene with 1% pyridine)[S1] was used as a standard for determination of fluorescence quantum yields. Low temperature absorption and emission measurements were made with the triple-grating TRIAX 320 spectrograph (focal length: 320 mm; aperture: *f*/4.1; dispersion: 4.6 nm/mm). The absorption spectrum was captured using 600 gr/mm blazed at 1000 nm grating with 0.05 mm slit, 3 ms exposure time and 20 accumulations by liquid N_2 cooled Symphony CCD detector (spectral range: 400–1000 nm). The emission spectra were recorded using the same grating with 0.3 mm slits and 1 s per 1 nm integration time by InGaAs solid state LN2 cooled detector (spectral range: 800–1500 nm). The estimated resolution is 0.23 nm for absorption and 1.38 nm for fluorescence. The wavelength calibration was performed with the HG-1 Mercury Argon Calibration Source (Ocean Optics, spectral range: 253–1700 nm) and the spectral response was calibrated with the LS-1-CAL calibrated tungsten halogen light source (Ocean Optics, 300–2000 nm). In absorption measurements, two spectra of halogen light source (DH – 2000, Micropack, UV-vis-NIR) focused on the entrance slit of spectrograph were measured. One spectrum was obtained by keeping the sample in the light path, another one was measured without the sample. The sample was excited using the 3900S CW tunable Ti: sapphire laser (tunable from 675 nm to 1000 nm) at the specified excitation wavelength and collected at 90 ° to the excitation beam. Analytical GPC was carried out using PLgel 3 μm Mixed-E columns (2 × 300 mm length, 7.5 mm diameter), with a flow rate of 1.0 mL/min.

Section S2. Synthetic procedures

3,5-Bis(*tert*-butyl)benzaldehyde,[S2] dipyrromethane,[S3] hexadentate template **T6**,[S1] porphyrin monomer ***l*-P'1**[S4] and linear porphyrin hexamer **Si$_2$-*l*-P'6**[S1] were synthesized according to published procedures. Although procedures for the synthesis of porphyrin monomer ***l*-P1** (Scheme S1) have been published before, we report optimized procedures here.

Scheme S1. Synthesis of porphyrin monomer ***l*-P1**.

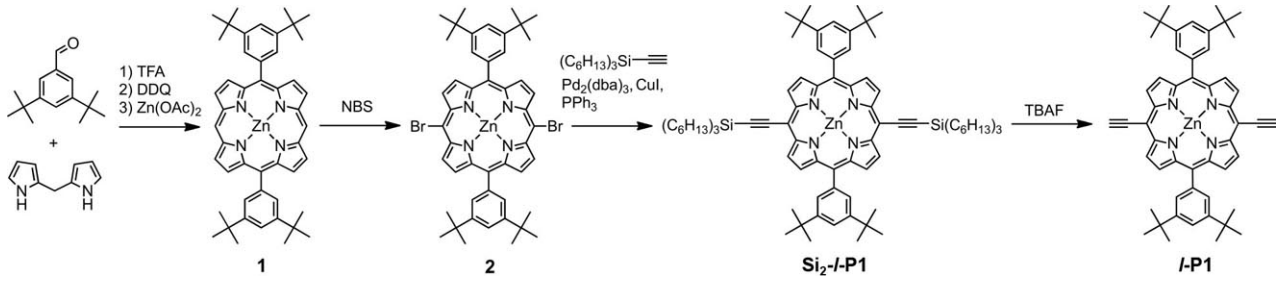

Zinc 5,15-bis-(3,5-bis-*tert*-butyl-phenyl)-porphyrin **1**

3,5-Bis(*tert*-butyl)benzaldehyde (1.79 g, 8.21 mmol) and dipyrromethane (1.20 g, 8.21 mmol) were placed in a dry flask under N_2 and dissolved in CH_2Cl_2 (1600 mL). The solution was degassed three times by repeated evacuation and purging with nitrogen. Trifluoroacetic acid (0.37 mL, 4.9 mmol) was added and the reaction mixture stirred in the dark for 3 h. DDQ (2.42 g, 10.7 mmol) was added and stirring continued for 0.5 h. After quenching of the acid by addition of triethylamine (8 mL) the mixture was passed over a short silica plug (CH_2Cl_2). After evaporation, the residue was dissolved in $CHCl_3$ (150 mL) and treated with a solution of zinc acetate dihydrate (1.80 g, 8.21 mmol) in MeOH (15 mL). After stirring the solution for 1 h at room temperature, the volume was reduced and the mixture passed over a silica plug (CH_2Cl_2/pyridine = 10/1). Recrystallization from CH_2Cl_2/MeOH gave porphyrin **1** as a red solid (1.73 g, 56%). ^{1}H NMR (400 MHz, $CDCl_3$): δ_H 1.59 (s, 36H, *t*Bu-*H*),7.86 (t, J = 2.0 Hz, -ArylH_{para}), 8.17 (d, J = 2.0 Hz, 4H, -ArylH_{ortho}), 9.23 (d, J = 4.5 Hz, 4H, -PorphH_β), 9.45 (d, J = 4.5 Hz, 4H, -PorphH_β), 10.36 (s, 2H, -PorphH_{meso}) (as literature).[S5]

Zinc 5,15-bis-(3,5-bis-*tert*-butyl-phenyl)-10,20-dibromo-porphyrin **2**

To a solution of zinc porphyrin **1** (1.2 g, 8.2 mmol) in $CHCl_3$ (190 mL) and pyridine (0.8 mL) was added dropwise *N*-bromosuccinimide (0.61 g, 3.4 mmol) dissolved in $CHCl_3$ (30 mL). After stirring in the dark for 15 minutes, the reaction was quenched with acetone (1.0 mL). The solvent was removed and the crude product recrystallized from CH_2Cl_2/MeOH to give dibromoporphyrin **2** as a purple solid (1.36 g, 92%). ^{1}H NMR (400 MHz, $CDCl_3$): δ_H 1.50 (s, 36H, *t*Bu-*H*),7.80 (t, J = 2.0 Hz, -ArylH_{para}), 7.99 (d, J = 2.0 Hz, 4H, -ArylH_{ortho}), 8.91 (d, J = 4.5 Hz, 4H, -PorphH_β), 9.66 (d, J = 4.5 Hz, 4H, -PorphH_β) (as literature).[S5]

Zinc 5,15-bis-(3,5-bis-*tert*-butyl-phenyl)-10,20-bis-trihexylsilanylethynyl-porphyrin **Si$_2$-*l*-P1**

tris-(Dibenzylideneacetone)-di-palladium(0) (64 mg, 70 μmol), copper(I) iodide (28 mg, 0.14 mmol), triphenylphosphine (36 mg, 0.14 mmol) and dibromoporphyrin **2** (0.64 g, 0.7 mmol) were placed in a dried Schlenk tube under argon. Toluene (45 mL), *i*Pr$_2$NH (24 mL) and pyridine (1.27 mL) were added and the reaction mixture deoxygenated. Trihexylsilyl acetylene (0.81 mL, 2.1 mmol) was added by syringe. The reaction mixture was stirred at 80 °C for 3 hours, solvents removed and the residue passed through a short silica gel column using CH_2Cl_2. Recrystallization by layer addition (CH_2Cl_2 / MeOH) gave the product **Si$_2$-*l*-P1** as a green solid (0.96 g, 99 %). ^{1}H

NMR (400 MHz, $CDCl_3$): δ_H 1.02 (m, 12H, hexyl-*H*), 1.39 (m, 24H, hexyl-*H*), 1.58–1.51 (m, 48H, 12 hexyl-*H*, 36 *t*Bu-*H*), 1.77 (m, 12H, hexyl-*H*), 7.83 (t, 2H, J = 1.5 Hz, -ArylH_{para}), 8.06 (d, 4H, J = 1.5 Hz, -ArylH_{ortho}), 8.98 (d, 4H, J = 4.5 Hz, -PorphH_{β}), 9.74 (d, 4H, J = 4.5 Hz, -PorphH_{β}) (as literature).[S6]

Zinc 5,15-bis-(3,5-bis-*tert*-butyl-phenyl)-10,20-bis-ethynyl-porphyrin ***l*-P1**

THS-protected porphyrin monomer **Si$_2$-*l*-P1** (100 mg, 73.3 μmol) was dissolved in CH_2Cl_2 (10 mL) and tetra-*n*-butylammonium fluoride (0.70 mL of a 1.0 M solution in THF) was added. After stirring at room temperature for 15 minutes the mixture was immediately passed through a short plug of silica gel (CH_2Cl_2). Recrystallization by layer addition (CH_2Cl_2 / MeOH) gave the product ***l*-P1** as a dark green solid (54 mg, 92 %). ^{1}H NMR (400 MHz, $CDCl_3$): δ_H 1.55 (s, 36H, *t*Bu-*H*), 4.15 (s, 2H, C≡C–*H*), 7.79 (t, 2H, J = 1.5 Hz, -ArylH_{para}), 8.01 (d, 4H, J = 1.5 Hz, -ArylH_{ortho}), 8.91 (d, 4H, J = 4.5 Hz, -PorphH_{β}), 9.67 (d, 4H, J = 4.5 Hz, -PorphH_{β}) (as literature).[S6]

Section S3. Solution-phase small angle X-ray scattering (SAXS)

Synchrotron radiation SAXS data were collected using standard procedures on the I22 beamline at the Diamond Light Source (UK) equipped with a photon counting detector. The beam was focused onto the detector placed at a distance of 1.25 m from the sample cell. The covered range of momentum transfer was $0.03 < q < 1.0$ Å^{-1} ($q = 4\pi\sin(\theta)/\lambda$ where 2θ is the scattering angle and λ = 1.00 Å is the X-ray wavelength). The data were normalized to the intensity of the incident beam; the scattering of the solvent was subtracted using an in-house program. To check for radiation damage during the SAXS experiment, the data were collected in 10 successive 60 s frames. All SAXS measurements were performed in either toluene or toluene/1% pyridine at known concentrations (~10^{-4} M) in a solution cell with mica windows (1 mm path length). Simulated scattering curves from molecular models were obtained by fitting to the experimental scattering data using the program CRYSOL.[S7] The program GNOM[S8] was used to calculate pair distribution functions and radii of gyration from experimental and simulated scattering data.

Table S1. Radii of gyration R_g determined from the experimental scattering data from Figure 3 in the main text using the program GNOM.[S8]

Compound	R_g (exp)	R_g (model)
***c*-P6·T6**	12.9 Å	12.4 Å
***c*-P6**	14.3 Å	13.2 Å
Si$_2$-*l*-P'6	23.8 Å	23.8 Å

Section S4. Electrochemistry

Electrochemical experiments on ***c*-P6·T6** and ***c*-P6** were performed using an Autolab PGSTAT12 potentiostat. Compounds were studied in freshly distilled THF containing Bu_4NBF_4 (0.1 M), under helium. Voltammograms were also recorded in THF containing 1% pyridine (volume ratio) and Bu_4NBF_4 (0.1 M). A 3 mm glassy carbon working electrode was used with a Pt wire counter electrode and an $Ag/AgNO_3$ reference electrode. The redox potentials of all the compounds were measured using square-wave voltammetry; the reversibility of the redox waves was checked by cyclic voltammetry. All the voltammograms were referenced to internal ferrocene (Fc/Fc^+ at 0 V).

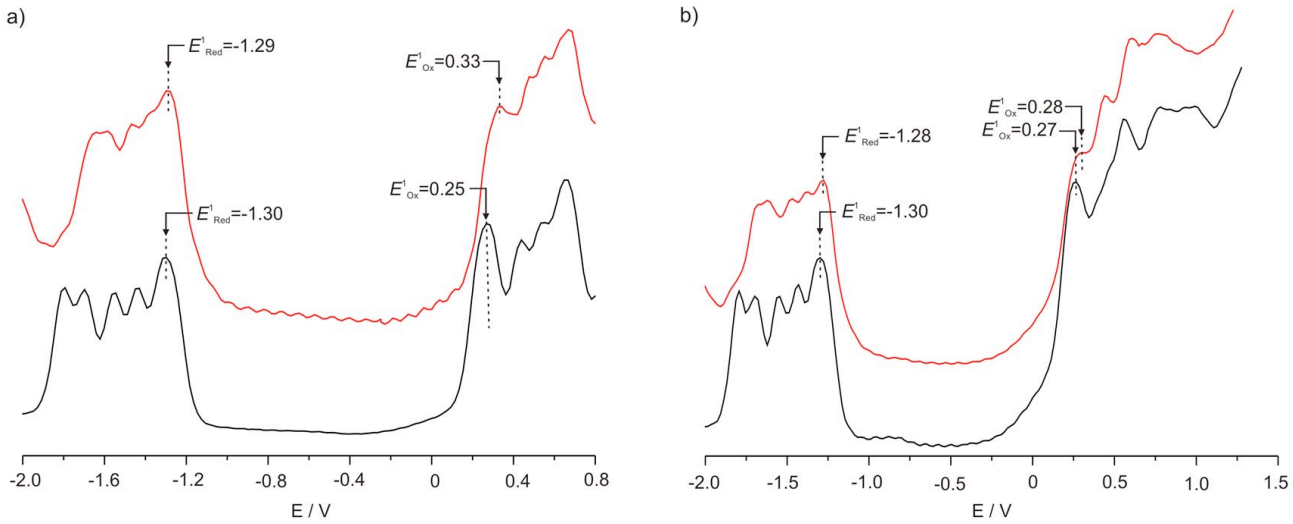

Figure S1. Square-wave voltammograms recorded for ***c*-P6·T6** (black curves) and ***c*-P6** (red curves) (a) in THF with 0.1 M Bu_4NPF_6 and (b) in THF containing 1% pyridine and 0.1 M Bu_4NPF_6 (square wave frequency 8 Hz; glassy carbon working electrode, Pt counter electrode, $Ag/AgNO_3$ reference electrode). All the voltammograms are referenced to internal ferrocene (Fc/Fc^+ at 0.00 V).

Section S5. Absorption and fluorescence spectroscopy

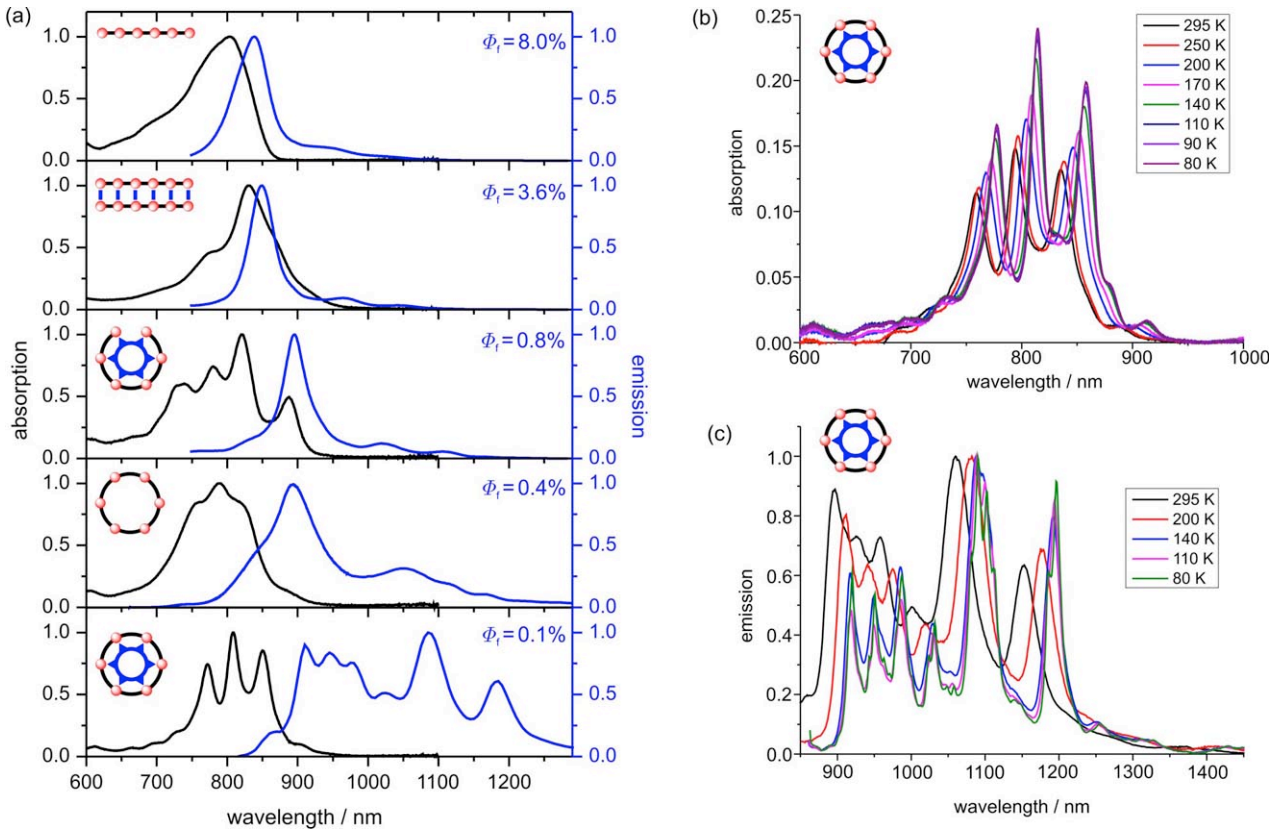

Figure S2. (a) Absorption (black line) and emission (blue line, excitation at 489 nm) spectra of (from top to bottom) **Si_2-*l*-P'6** in toluene/1% pyridine, **(Si_2-*l*-P'6)$_2$·(4,4'-bipyridine)$_6$** in toluene, **Si_2-*l*-P'6·T6** in toluene, ***c*-P6** in toluene/1% pyridine and ***c*-P6·T6** in toluene; b) Absorption spectra of ***c*-P6·T6** in methylcyclohexane at temperatures between 295 and 80 K. c) Emission spectra of ***c*-P6·T6** in methylcyclohexane at temperatures between 295 and 80 K (excited at 835–858 nm, moving with the maximum of the absorption peak, see (b).

Identification of peaks in the fluorescence spectrum of *c*-P6·T6 due to emissive impurities

The nanoring template complex ***c*-P6·T6** has a very low fluorescence quantum yield (Φ_f = 0.1%), thus traces of fluorescent impurities, which cannot be detected by other techniques, are often observed in the fluorescence spectrum of this compound. After assigning the majority of peaks in the fluorescence spectrum as S_0-S_1 HT transitions, several minor peaks remain unassigned. The relative intensity of these peaks increases after storing the sample for a few days, so we attribute these peaks to decomposition products. The fluorescence and excitation spectra of these impurities indicates that they are similar to **Si_2-*l*-P'6·T6**, i.e. with a single break in the π-system breaking the symmetry.

One fluorescence impurity peak occurs at higher energies than the predicted S_0-S_1 0-0 transition of ***c*-P6·T6** at 1.31 eV. This peak is observed at a wavelength of 916 nm in MCH at 80 K, 893 nm in MCH at 295 K and at 910 nm in toluene at 295 K (Figure S3b). The photoluminescence excitation (PLE) map in Figure S3a shows that emission at 910 nm contains a contribution from an impurity, because the vertical slice at 910 nm is different from vertical slices at other wavelengths and does not match the absorption spectrum of ***c*-P6·T6**. This conclusion is confirmed by comparison with the PLE map in Figure 3c, from a sample of ***c*-P6·T6** which contained less of the impurity and did not exhibit the same emission feature at 910 nm. Figure S3d shows the excitation spectra at emission wavelength 910 nm extracted from these two PLE maps: The excitation spectrum of the sample containing more impurity does not match the absorption spectrum, while very good overlap is found in the case of the purer sample.

The fluorescent impurity is particularly evident when samples of ***c*-P6·T6** are excited at the long wavelength edge of the absorption band, at 906 nm (1.36 eV), where the nanoring absorbs very weakly, as illustrated in Figure S4 (blue line). From the un-normalized emission spectra in Figure S4 it is clear that the intensity of these additional peaks is small compared to the emission spectra excited at shorter wavelength (where ***c*-P6·T6** absorption is stronger).

The fluorescence spectrum of ***c*-P6·T6** recorded at 295 K (Figure 7d) shows a shoulder at around 850 nm which disappears when the fluorescence spectrum is recorded at 80 K. Further experiments will be required to firmly assign this shoulder; it could be due to emission from an S_2 state or it could originate from conformations of the nanoring which are not populated at low temperatures.

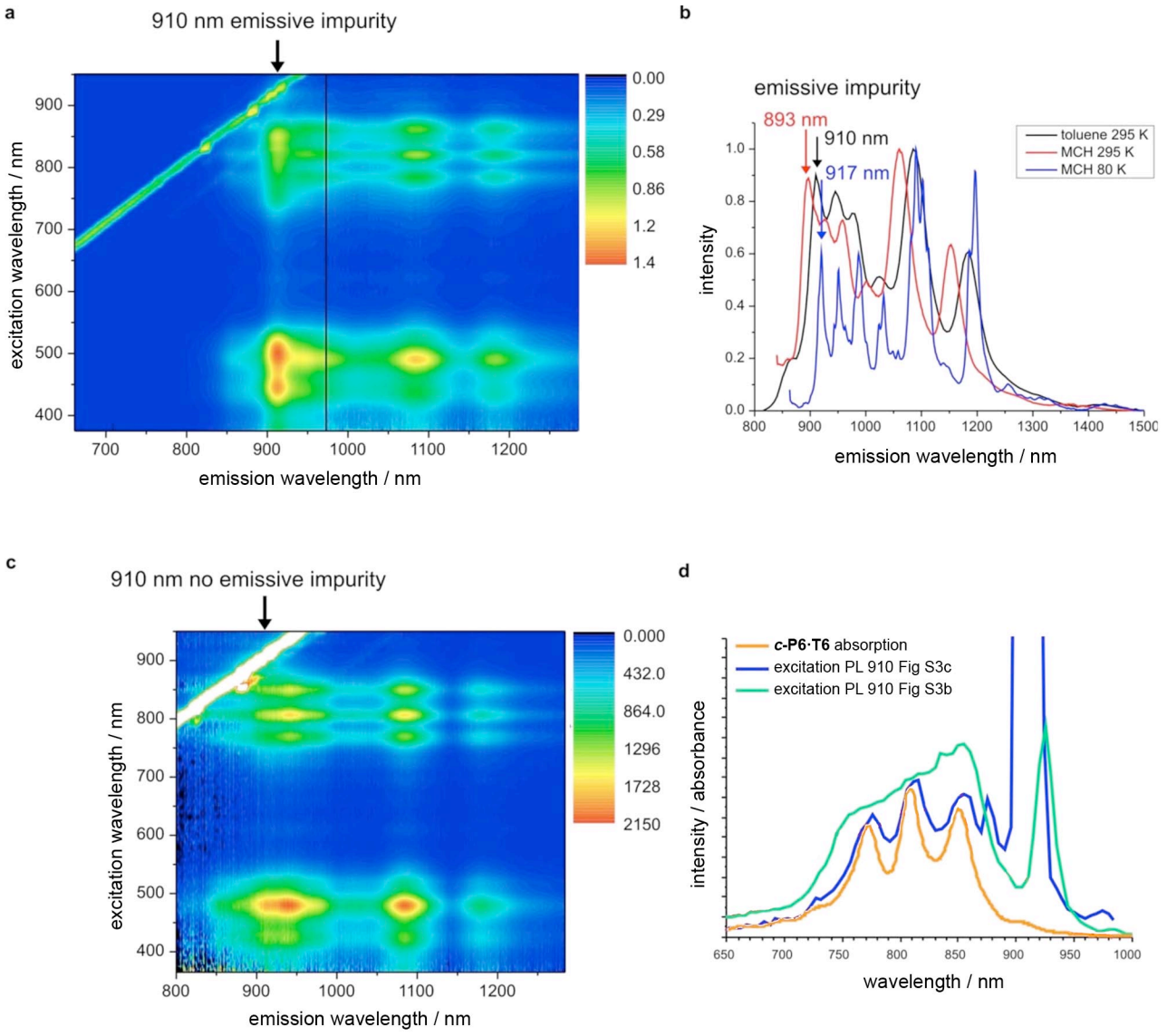

Figure S3. Identification of an emissive impurity in ***c*-P6·T6**, that is not detectable by UV-vis-NIR absorption or ^{1}H NMR. (a) Photoluminescence excitation (PLE) map of ***c*-P6·T6** in toluene. The difference in the excitation spectrum (vertical slice) at 910 nm compared to the excitation spectra at all other wavelengths allows the emission feature at this wavelength to be assigned to an emissive impurity. The PLE map was measured using a Si-diode CCD detector for shorter wavelengths and an InGaAs detector for longer wavelengths. The vertical black line shows where the two maps were joined. (b) Emission spectrum of ***c*-P6·T6** in toluene excited at 809 nm (black line) with the emission peak of the impurity at 910 nm marked with a black arrow; emission spectrum in methylcyclohexane (MCH) at 295 K upon excitation at 835 nm (red line) with the emissive impurity shifted to 893 nm (red arrow); emission spectrum in MCH at 80 K upon excitation at 858 nm (blue line) with the emissive impurity shifted to 917 nm (blue arrow); (c) PLE map of a sample of ***c*-P6·T6** in toluene in the absence of the emissive impurity; (d) excitation spectra for emission at 910 nm from maps (a) and (c) together with absorption spectra of ***c*-P6·T6**.

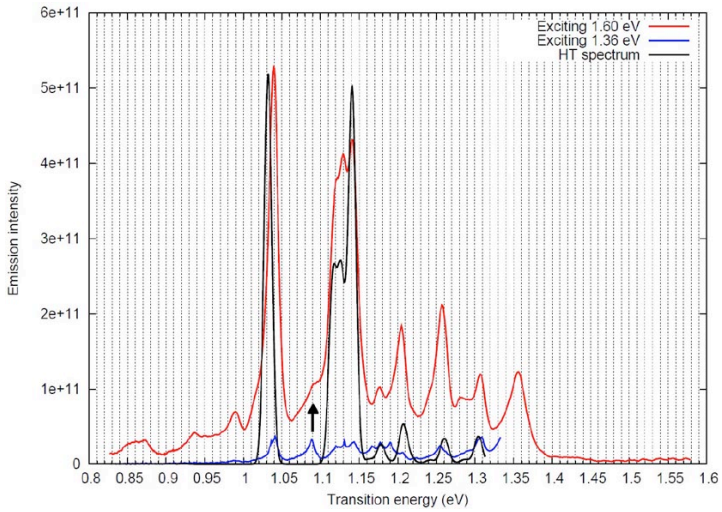

Figure S4. Un-normalized fluorescence spectra of ***c*-P6·T6** in methylcyclohexane at 78 K, excited at 1.6 eV (red) and 1.36 eV (blue) and simulated HT spectrum (black). Both experimental spectra seem to contain a peak at 1.09 eV, which is not predicted by the HT spectrum assuming a 0-0 of 1.31 eV. Focusing on the main peaks in both experimental spectra, it can be seen that the spectrum observed when exciting at 1.36 eV contains the same peaks obtained when exciting at 1.6 eV (the HT vibronic envelope of ***c*-P6·T6** S_0-S_1 transitions) as well as an echo of this vibronic envelope shifted 0.05 eV to the blue. We attribute this blue-shifted spectrum to HT transitions from S_1 of the decomposition product, which is selectively populated when exciting at 1.36 eV. Thus the peak at 1.09 eV is assigned to the strongest HT transition of the decomposition product.

Section S6. Time-Resolved Fluorescence Decay Measurements

Time-resolved photoluminescence (TRPL) measurements were conducted ***c*-P6·T6** in toluene (at a concentration of approximately 0.1 mM) using a femtosecond photoluminescence up-conversion setup. Solutions held in quartz cuvettes at room temperature were excited with laser pulses of center-wavelength 770 nm and fluence of 0.85 μJ cm^{-2} with frequency-doubled pulses of 100 fs duration originating from a mode-locked Ti:Sapphire oscillator. The emerging photoluminescence was collected by a pair of off-axis parabolic mirrors and focused onto a β-barium-borate (BBO) crystal mounted on a rotation stage to allow tuning of the phase-matching angle. An intense vertically polarized gate beam (center-wavelength 770 nm) arriving at the BBO crystal at adjustable time-delay was used to up-convert the photoluminescence at given times after excitation. The resulting sum-frequency photons were collected, dispersed in a monochromator, and detected by a liquid-nitrogen cooled CCD. The fluorescence decay curve is shown in Figure S5.

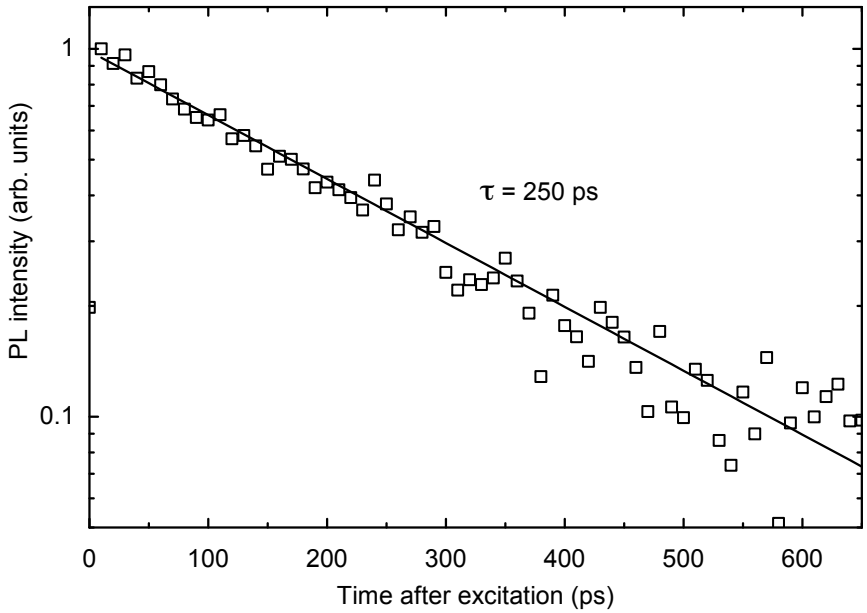

Figure S5. Fluorescence decay curve recorded for ***c*-P6·T6** in toluene using the femtosecond photoluminescence up-conversion setup (pulse duration: 100 fs; excitation wavelength: 770 nm; detection wavelength: 945 nm). These data yield a fluorescence lifetime of 250 ± 6 ps.

Section S7. Time-Resolved Fluorescence Anisotropy Measurements

Time-resolved fluorescence anisotropy measurements were conducted on **Si_2-*l*-P'6** and ***c*-P6** in toluene / 1% pyridine and ***c*-P6·T6** in toluene (at a concentration of approximately 0.1 mM) using a femtosecond photoluminescence up-conversion setup, as described above (Section S6). Only the vertical polarization component of the photoluminescence was up-converted in this setup; therefore, either the parallel ($PL_{\parallel}$) or the perpendicular ($PL_{\perp}$) luminescence polarization with respect to the excitation polarization was selected by changing the polarization of the excitation beam through rotation of a half-wave plate and a Glan-Thompson polarizer. The temporal resolution of the system was 800 fs. Figure S6 shows the resulting polarization anisotropy values r calculated from these data in the usual way, using $r = (PL_{\parallel} - PL_{\perp})/(PL_{\parallel} + 2PL_{\perp})$. Any initial drop in polarization anisotropy is too fast to resolve. Within the first few tens of picoseconds, no further drop in r is observed; constant average values of $r = 0.32 \pm 0.02$ are obtained for **Si_2-*l*-P'6**, which reduce to $r = 0.082 \pm 0.01$ and $r = 0.077 \pm 0.02$ for ***c*-P6·T6** and ***c*-P6**, respectively.

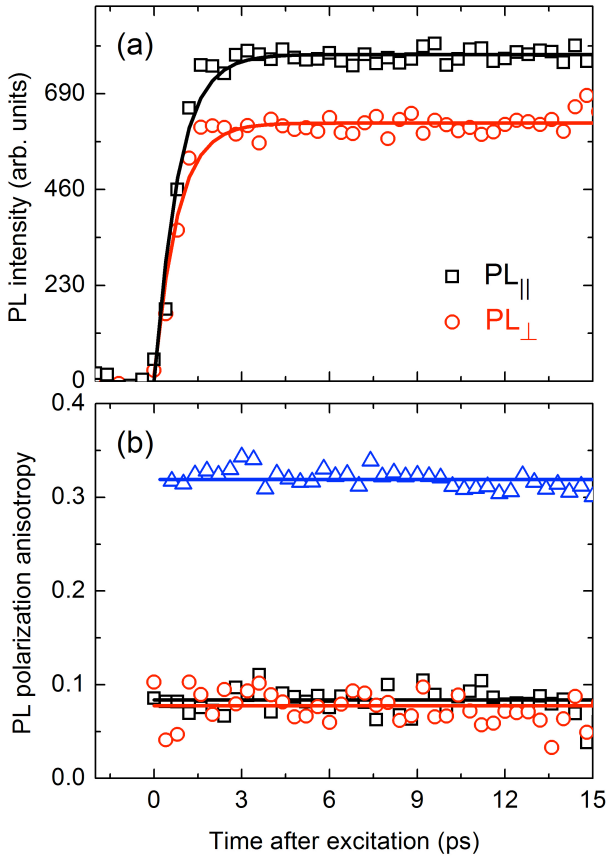

Figure S6. (a) PL components emitted with polarization parallel ($PL_{\parallel}$, black squares) or perpendicular ($PL_{\perp}$, red circles) to the excitation polarization for ***c*-P6·T6** in toluene containing 1% pyridine at a detection wavelength of 945nm. (b) Polarization anisotropy values r calculated from such data for **Si_2-*l*-P'6** (blue triangles, detection at 850 nm), ***c*-P6** (red circles, detection at 890 nm) in toluene containing 1% pyridine and ***c*-P6·T6** (black squares, detection at 945 nm) in toluene. The solid lines are average values calculated for the delay range of 0–15 ps, which are $r = 0.32 \pm 0.02$ for **Si_2-*l*-P'6**, $r = 0.082 \pm 0.01$ for ***c*-P6·T6** and $r = 0.077 \pm 0.02$ for ***c*-P6**.

Section S8. Computational Studies

Table S2. ***c*-P6·T6** (with aryl side groups removed) S_0-S_1 and S_0-S_2 oscillator strengths f, electronic transition energies ω and their relative transition energies calculated using several methods affordable for a molecule of this size. Geometries were previously optimized while constraining the symmetry to D_6 using Turbomole. TD-DFT calculations were performed using Gaussian 09 apart from those highlighted with an asterisk which were performed using Turbomole. The 6-31g(d,p) basis set was used for all DFT calculations. INDO/SCI calculations were performed using an in-house program using an active space of 120 occupied and unoccupied orbitals. [+] Using this model, an additional dark state appeared above S_1 such that the strongly allowed state for which the transition energy is reported is in fact S_3.

Geometry	Method	ω S_0-S_1 (eV)	ω S_0-S_2 (eV)	Spacing (eV)	f S_0-S_1	f S_0-S_2
B3LYP	TD-B3LYP*	1.060	1.475[+]	0.415	0.000	5.489
B3LYP	INDO/SCI	1.513	1.633	0.120	0.000	1.823
B3LYP	TD-LC-wPBE	1.360	1.599	0.240	0.000	3.091
BHLYP	TD-BHLYP	1.601	1.864	0.262	0.000	4.506
BHLYP	TD-BHLYP*	1.600	1.863	0.263	0.000	4.353
BHLYP	INDO/SCI	1.622	1.711	0.089	0.000	1.220

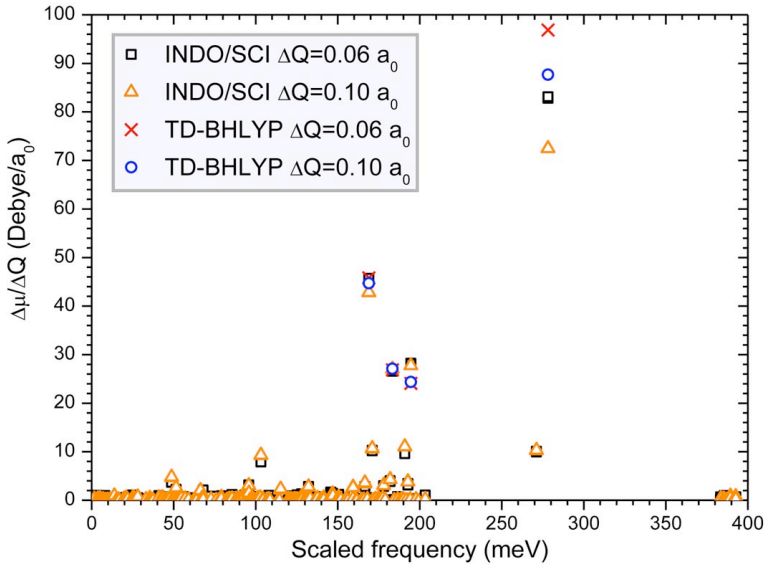

Figure S7. Numerical S_0-S_1 HT transition dipole moment derivatives $\Delta\mu/\Delta Q$ with respect to displacement along modes of e_1 symmetry. Derivatives were calculated for all modes of e_1 symmetry using two displacements ΔQ of 0.06 (black squares) and 0.1 (orange triangles) Bohr Radii (a_0) at the INDO/SCI level. Derivative calculations were repeated at the TD-BHLYP level for one component of each of the 4 pairs of double degenerate modes most strongly coupled. TD-BHLYP derivatives for displacements ΔQ of 0.06 (red crosses) and 0.1 (blue circles) a_0 are in excellent agreement with INDO/SCI derivatives for three of the four most strongly coupled modes while for the most strongly coupled mode the agreement is acceptable. Additionally, for all but the most strongly coupled mode, the value of derivatives is almost identical for displacements of 0.06 and 0.1 a_0, indicating the suitability of the linear HT approximation. Derivatives were calculated by evaluating the change in the magnitude of the S_0-S_1 transition dipole moment relative to the D_6 symmetric ground state geometry, i.e. $\Delta\mu/\Delta Q = (|\mu_{e1}|-|\mu_{D6}|)/\Delta Q$ where μ_{e1} and μ_{D6} are the S_0-S_1 transition dipole moments in the distorted and D_6 ground state geometries respectively.

Radiative Rate Constants. Einstein spontaneous emission rates were calculated for individual HT transitions using the equation:

$$k_{rad} = \frac{4}{3}\frac{|\mu|^2}{4\pi\varepsilon_0\hbar}\left(\frac{\omega}{c}\right)^3 = \frac{|\mu|^2\,\omega^3}{6077}$$

where μ and ω are the transition dipole moment and frequency of the transition respectively, ε_0 is the dielectric permittivity of vacuum, $\hbar$ is the reduced Planck constant and c is the speed of light in vacuum. The expression on the right yields k_{rad} in ns^{-1} if μ and ω are given in Debye and eV respectively. Rates for individual transitions can be seen in Figure 10 of the main text. Radiative decay rates of individual HT transitions were summed to yield S_0-S_1 radiative decay rates (see Table S3) comparable with experimental radiative decay rates. Comparing the rates obtained by summing over the most strongly coupled 8 modes and by summing over all e_1 modes indicates that the most strongly coupled 8 modes account for more than 80% of the radiative decay at the INDO/SCI level. Comparing the summed rate of the most strongly coupled 8 modes calculated from INDO/SCI and TD-BHLYP calculations indicates that INDO/SCI recovers over 85% of the decay rate predicted by the higher level TD-BHLYP calculations. Our HT models thus predict a total radiative decay rate of approximately 10^7 s^{-1}, as compared to the experimental radiative lifetime obtained from the ratio of fluorescence quantum yield Φ_{f} (0.0012) over fluorescence lifetime τ_{f} (250 ps) of 4.8×10^6 s^{-1}. Radiative decay rates of the purely electronic transitions without HT contributions are listed in Table S4. Transitions from S_1 and S_2 to the S_0 ground state occur at rates in the range 10^3–10^4 and 10^8–10^9 s^{-1} respectively and are thus too slow and too fast respectively to account for the experimental radiative decay rates. Though our HT intensities are slightly overestimated, considering the complexity of the system and the approximations made the agreement is excellent.

Table S3. Comparison of summed Einstein spontaneous emission radiative decay rates k_{rad} using different quantum chemical methods (INDO/SCI and TD-BHLYP), numbers of modes (8 most strongly coupled modes or all e_1 modes) and displacements ΔQ used for numerical evaluation of $\Delta\mu/\Delta Q$ HT derivatives (0.06 or 0.1 a_0).

Model	**ΔQ in $\Delta\mu/\Delta Q$ (a_0)**	**k_{rad} (s^{-1})**
TD-BHLYP 8 modes	**0.06**	7.83×10^6
TD-BHLYP 8 modes	**0.1**	7.08×10^6
INDO/SCI 8 modes	**0.06**	7.08×10^6
INDO/SCI 8 modes	**0.1**	6.18×10^6
INDO/SCI all modes	**0.06**	8.42×10^6
INDO/SCI all modes	**0.1**	7.56×10^6
Models compared		**Fraction**
INDO/SCI 8 modes / all modes	**0.06**	0.84
INDO/SCI 8 modes / all modes	**0.1**	0.82
8 modes INDO/SCI / TD-BHLYP	**0.06**	0.91
8 modes INDO/SCI / TD-BHLYP	**0.1**	0.87

Table S4. Einstein spontaneous emission radiative decay rates k_{rad} for electronic transitions between S_1, $S_2(x)$ and $S_2(y)$ and the ground state S_0.

Model	Transition	ω (eV)	μ (Debye)	k_{rad} (s^{-1})
TD-BHLYP	S_1-S_0	1.601	0.083	4.7×10^3
TD-BHLYP	$S_2(x)$-S_0	1.864	17.855	3.4×10^8
TD-BHLYP	$S_2(y)$-S_0	1.864	17.855	3.4×10^8
INDO/SCI	S_1-S_0	1.622	0.154	1.7×10^4
INDO/SCI	$S_2(x)$-S_0	1.711	9.690	7.7×10^7
INDO/SCI	$S_2(y)$-S_0	1.711	9.670	7.7×10^7

Section S9. Crystallography of *c*-P6·T6

General Crystallographic Details. Crystals of ***c*-P6·T6** were grown by vapor diffusion of *n*-hexane into a solution in 1% pyridine/$CHCl_3$. Diffraction data were collected at 150 K using synchrotron X-ray radiation at the Diamond Light Source, beamline I19 (EH1). The structure was solved using SuperFlip[S9] and refined using full-matrix least-squares within the CRYSTALS software suite.[S10] The asymmetric unit contains 0.5 molecules of ***c*-P6·T6** and there is a crystallographic inversion center at the center of the molecule.

A second polymorph was also observed, as black hexagonal plates with a cell of a = 49.85 Å, c = 29.46 Å, V = 63395 $Å^3$. This polymorph was persistent and was seen on many occasions. The unique axis length was found to vary, perhaps as a function of solvation. Although the structure was never solved, it is postulated to consist of flat layers with pseudo 6-fold symmetry caused by the ***c*-P6-T6** forming a hexagonal array. Ordering between the ***c*-P6·T6** layers (separated by solvent) is poor, leading to a two dimensional diffraction pattern that failed to solve.

Crystal packing. The nanoring molecules are arranged in layers, in a side-to-face herringbone fashion (Figure S8).

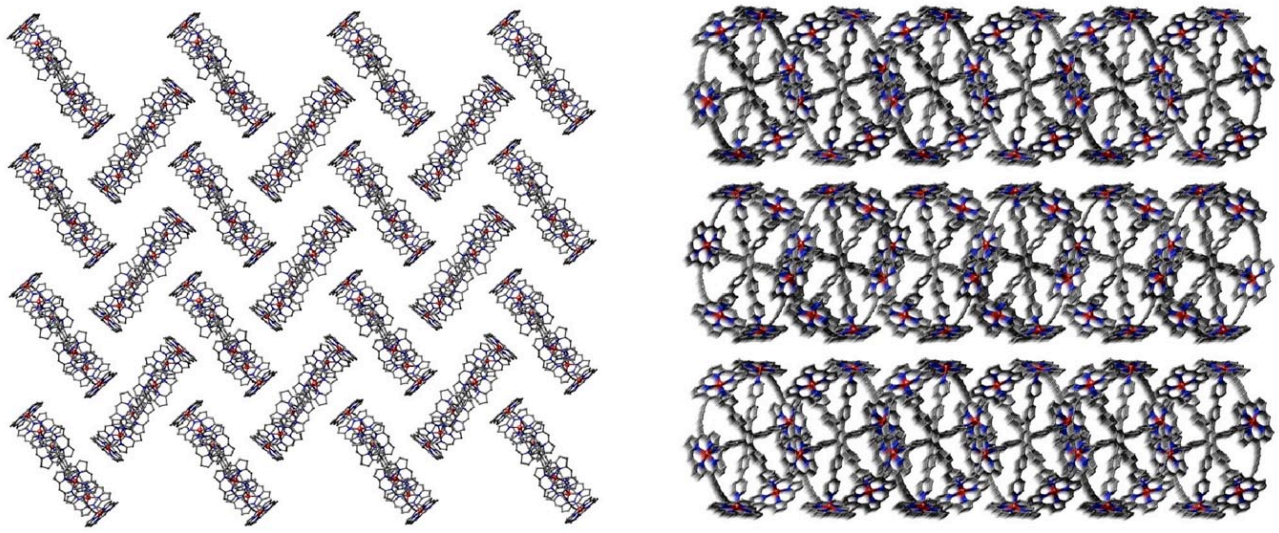

Figure S8. The packing diagram for ***c*-P6·T6** showing two orthogonal views of the crystal structure. Hydrogen atoms, solvent molecules and aryl side groups have been omitted for clarity.

Conformation of the nanoring. Molecules of ***c*-P6·T6** in the crystal are slightly distorted from ideal D_{6h} symmetry having a clear 'chair-like' geometry (Figure 4). The butadiyne carbons lie significantly away from the mean plane of the six Zn-centers [mean deviation distances are 0.81 Å (C_α) and 0.86 Å (C_β), calculated using the CrystalMaker software, version 7.2.4]. The six porphyrins are essentially planar: the sum of RMS deviations for the 24 atoms of the porphyrin core, averaged over three crystallographically non-equivalent porphyrin units, is only 0.023 Å which is even lower than the value in unstrained porphyrin dimer **Si_2-*l*-P2** (0.043 Å).[S11] The 'sum of RMS deviations for the 24 atoms of the porphyrin core' was defined as the square root of sum-of-squares of out-of-plane distances of the 20 carbon atoms and four nitrogen atoms of the porphyrin core from the mean plane of these 24 atoms (calculated using the CrystalMaker software).

Distortion of the porphyrin units. The strain in the porphyrin units pulls the 5 and 15 *meso* carbon atoms away from the plane of the porphyrin, whereas the 10 and 20 carbon atoms lie in the plane of the porphyrin, as in a typical 5-coordinate Zn-porphyrin pyridine complexes. This distortion is easily seen by comparing the angles between *meso*-positions and the centroid of four pyrrole nitrogens (Figure 5c). The distortion of the porphyrin has little influence on the coordination sphere of the Zn-center: the mean distances from the Zn-atom to the 24-atom porphyrin core (0.290 Å) and from the Zn-atom to pyridine nitrogen (2.145 Å) in ***c*-P6·T6** are close to those found in typical 5-coordinate Zn-porphyrin pyridine complexes (Figure 5a,b). Only porphyrins with no substituents in *β*- and adjacent *meso*-positions have been included in this search; porphyrins with bulky substituents in *meso*-positions were also excluded. A search of the Cambridge Crystallographic Database (CSD, Version 5.32 with the Nov. 2010 update)[S12] produced 111 hits and was performed using the software ConQuest (version 1.12).[S13] The porphyrin plane was fitted through the 20 carbon atoms and 4 nitrogen atoms of the porphyrin core. Data were analyzed using program Vista.[S14]

Geometry of the butadiyne units. Most of the strain in ***c*-P6·T6** is distributed among acetylenes, resulting in significant bending. This bending is quantified by the angles θ_1 (C_{sp2}-C_α≡C_β) and θ_2 (C_α≡C_β-C_β). The six non-equivalent values of θ_1 and θ_2 in ***c*-P6·T6** are compared with values for acyclic and cyclic 1,3-butadiynes in the CSD in Figure 5d. The search of the CSD for acyclic 1,3-

butadiynes produced 177 hits; that for cyclic species produced 149 hits. Only the butadiyne fragments connected to sp^2-carbon atoms were included in this analysis; those with triple bonds coordinated to metals were excluded. The two types of bond angles appear to be equally flexible; their mean values in ***c*-P6·T6** are similar (θ_1: 169.6 ± 1.7 °; θ_2: 170.5 ± 1.6 °). There is a negative correlation between θ_1 and θ_2, thus the sum $\theta_1 + \theta_2$ has less scatter and is a better measure of angle strain than either θ_1 or θ_2. The bending of the butadiyne units in ***c*-P6·T6** is less extreme than that reported for some cyclic molecules containing 1,3-butadiyne links.

Section S10. Full list of authors for reference 45

(45) Gaussian 09, Revision A.02, Frisch, M. J.; Trucks, G. W.; Schlegel, H. B.; Scuseria, G. E.; Robb, M. A.; Cheeseman, J. R.; Scalmani, G.; Barone, V.; Mennucci, B.; Petersson, G. A.; Nakatsuji, H.; Caricato, M.; Li, X.; Hratchian, H. P.; Izmaylov, A. F.; Bloino, J.; Zheng, G.; Sonnenberg, J. L.; Hada, M.; Ehara, M.; Toyota, K.; Fukuda, R.; Hasegawa, J.; Ishida, M.; Nakajima, T.; Honda, Y.; Kitao, O.; Nakai, H.; Vreven, T.; Montgomery, Jr., J. A.; Peralta, J. E.; Ogliaro, F.; Bearpark, M.; Heyd, J. J.; Brothers, E.; Kudin, K. N.; Staroverov, V. N.; Kobayashi, R.; Normand, J.; Raghavachari, K.; Rendell, A.; Burant, J. C.; Iyengar, S. S.; Tomasi, J.; Cossi, M.; Rega, N.; Millam, N. J.; Klene, M.; Knox, J. E.; Cross, J. B.; Bakken, V.; Adamo, C.; Jaramillo, J.; Gomperts, R.; Stratmann, R. E.; Yazyev, O.; Austin, A. J.; Cammi, R.; Pomelli, C.; Ochterski, J. W.; Martin, R. L.; Morokuma, K.; Zakrzewski, V. G.; Voth, G. A.; Salvador, P.; Dannenberg, J. J.; Dapprich, S.; Daniels, A. D.; Farkas, Ö.; Foresman, J. B.; Ortiz, J. V.; Cioslowski, J.; Fox, D. J. Gaussian, Inc., Wallingford CT, 2009.

Section S10. References

(S1) Hoffmann, M.; Kärnbratt, J.; Chang, M.-H.; Herz, L. M.; Albinsson, B.; Anderson, H. L. *Angew. Chem. Int. Ed.* **2008**, *47*, 4993–4996.

(S2) Newman, M. S.; Lee, L. F. *J. Org. Chem.* **1972**, *37*, 4468–4469.

(S3) Littler, B. J.; Miller, M. A.; Hung, C.-H.; Wagner, R. W.; O'Shea, D. F.; Boyle, P. D.; Lindsey, J. S. *J. Org. Chem.* **1999**, *64*, 1391–1396.

(S4) Winters. M. U.; Dahlstedt, E.; Blades, H. E.; Wilson, C. J.; Frampton, M. J.; Anderson, H. L.; Albinsson, B. *J. Am. Chem. Soc.* **2007**, *129*, 4291–4297.

(S5) Plater, M. J.; Aiken, S.; Bourhill, G. *Tetrahedron* **2002**, *58*, 2405–2413.

(S6) Taylor, P. N.; Anderson, H. L. *J. Am. Chem. Soc.* **1999**, *121*, 11538–11545.

(S7) Svergun, D. I.; Berbato, C.; Koch, M. H. J. *J. Appl. Cryst.* **1995**, *28*, 768–773.

(S8) Svergun, D. I. *J. Appl. Cryst.* **1992**, *25*, 495–503.

(S9) Palatinus, L.; Chapuis, G. *J. Appl. Cryst.* **2007**, *40*, 786–790.

(S10) Betteridge, P. W.; Carruthers, J. R.; Cooper, R. I.; Prout, K.; Watkin, D. J. *J. Appl. Cryst.* **2003**, *36*, 1487.

(S11) Taylor, P. N.; Huuskonen, J.; Rumbles, G.; Aplin, R. T.; Williams, E.; Anderson, H. L. *Chem. Comm.* **1998**, 909–910.

(S12) Allen, F. H. *Acta Cryst.* **2002**, *B58*, 380–388.

(S13) Bruno, I. J.; Cole, J. C.; Edgington, P. R.; Kessler, M.; Macrae, C. F.; McCabe, P.; Pearson, J.; Taylor, R. *Acta Cryst.* **2002**, *B58*, 389–397.

(S14) CCDC (1994). Vista - A Program for the Analysis and Display of Data Retrieved from the CSD. Cambridge Crystallographic Data Centre, 12 Union Road, Cambridge, UK.